THE RAPIDLY ROTATING SUN

Shravan M. Hanasoge [*] [†] **and Thomas L. Duvall, Jr.** [‡] **and Katepalli R. Sreenivasan** [§]

[*]Department of Geosciences, Princeton University, NJ 08544, USA,[†]Max-Planck-Institut für Sonnensystemforschung, 37191 Katlenburg-Lindau, Germany,[‡]Solar Physics Laboratory, NASA/Goddard Space Flight Center, MD 20771, USA, and [§]Courant Institute of Mathematical Sciences, New York University, NY 10012, USA

Submitted to Proceedings of the National Academy of Sciences of the United States of America

Convection in the solar interior is thought to comprise structures at a continuum of scales, from large to small. This conclusion emerges from phenomenological studies and numerical simulations though neither covers the proper range of dynamical parameters of solar convection. In the present work, imaging techniques of time-distance helioseismology applied to observational data reveal no long-range order in the convective motion. We conservatively bound the associated velocity magnitudes, as a function of depth and the spherical-harmonic degree ℓ, to be 20-100 times weaker than prevailing estimates within the wavenumber band $\ell < 60$. The observationally constrained kinetic energy is approximately a thousandth of the theoretical prediction, suggesting the prevalence of an intrinsically different paradigm of turbulence. A fundamental question arises: what mechanism of turbulence transports the heat flux of a solar luminosity outwards? The Sun is seemingly a much faster rotator than previously thought, with advection dominated by Coriolis forces at scales $\ell < 60$, with Rossby numbers smaller than $\sim 10^{-2}$ at $r/R_\odot = 0.96$. The Taylor-Proudman theorem is valid in this regime, and given that iso-rotation contours in the Sun are not co-aligned with the axis of rotation, a latitudinal entropy gradient is necessitated.

The thin photosphere of the Sun, where thermal transport is dominated by free-streaming radiation, shows a spectrum in which granulation and supergranulation are most prominent. Observed properties of granules, such as spatial scales, radiative intensity and line formation are successfully reproduced by numerical simulations [1, 2]. In contrast, convection in the interior is not directly observable and likely governed by aspects more difficult to model, such as the integrity of descending plumes and various instabilities [3]. Further, solar convection is governed by extreme parameters [4] (Prandtl number $\sim 10^{-6} - 10^{-4}$, Rayleigh number $\sim 10^{19} - 10^{24}$, and Reynolds number $\sim 10^{12} - 10^{16}$), which make three-dimensional direct numerical simulations impossible for the foreseeable future. It is likewise difficult to reproduce them in laboratory experiments.

Turning to phenomenology, mixing-length theory (MLT) is predicated on the assumption that parcels of fluid of a specified velocity scale transport heat over one length scale (termed the *mixing length*) and are then mixed in the new environment. While this picture is simplistic [5], it has been successful in predicting aspects of solar structure as well as the dominant scale and magnitude of observed surface velocities. MLT predicts a spatial convective scale that increases with depth (while velocities reduce) and coherent large scales of convection, termed *giant cells*. Simulations of anelastic global convection [6, 7], more sophisticated than MLT, support the classical picture of a turbulent cascade. Considerable effort has been spent in attempting surface [8] and interior detection [9, 10] of giant cells, but evidence supporting their existence has remained inconclusive.

Here, we image the solar interior using time-distance helioseismology [9, 10, 11]. Raw data in this analysis are line-of-sight photospheric Doppler velocities measured by Helioseismic and Magnetic Imager [12] onboard the Solar Dynamics Observatory. Two-point correlations from temporal segments of length T of the observed Doppler wavefield velocities are formed and spatially averaged according to a deep-focusing geometry [13] (Figures 1 and 2). We choose T based on estimates of convective coherence timescales [14, 15, 6]. These correlations are then fitted to a reference Gabor wavelet function [16] to obtain travel-time shifts $\delta\tau(\theta, \phi, T)$, where (θ, ϕ) are co-latitude and longitude on the observed solar disk. By construction, these time shifts are sensitive to different components of 3D vector flows, i.e., longitudinal, latitudinal or radial, at specific depths of the solar interior ($r/R_\odot = 0.92, 0.96$) and consequently, we denote individual flow components (longitudinal or latitudinal) by scalars. Each point (θ, ϕ) on the travel-time map is constructed by correlating 10,000 points, ...()NUMBER of correlations + measurements. A sample travel-time map is shown in Figure 3.

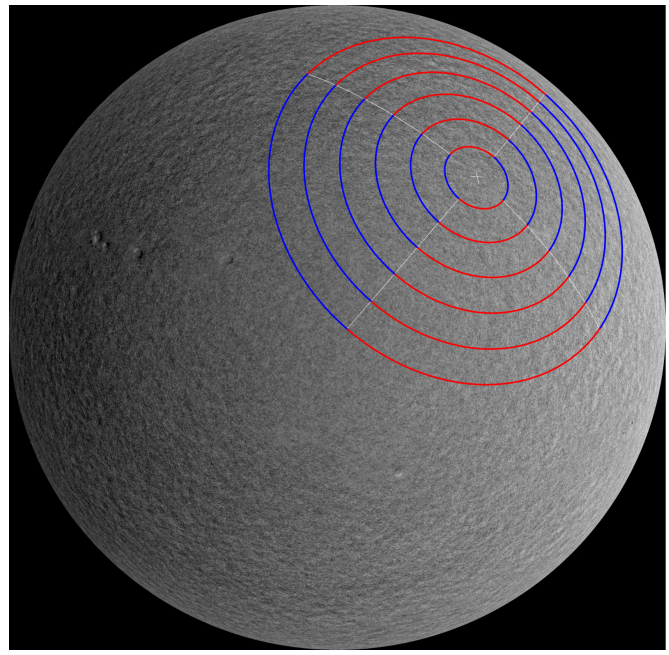

Fig. 1. Line-of-sight Doppler velocities are measured every 45 seconds at 4096×4096 pixels on the solar photosphere by the Helioseismic and Magnetic Imager (background image). We cross correlate wavefield records of temporal length T at points on opposing quadrants (blue with blue or red with red). These "blue" and "red" correlations are separately averaged, respectively sensitive to longitudinal and latitudinal flow at $(\theta, \phi; r/R_\odot = 0.96)$, where (θ, ϕ) is the central point marked by a cross (see Figure 2 for further illustration). The longitudinal measurement is sensitive to flows in that direction while the latitudinal measurement to flows along latitude. We create a travel-time maps $\delta\tau(\theta, \phi, T)$ by making this measurement at various points on the surface.

Waves are stochastically excited in the Sun, because of which the above correlation and travel-time measurements include components of incoherent wave noise, whose variance [17] diminishes as T^{-1}.

Reserved for Publication Footnotes

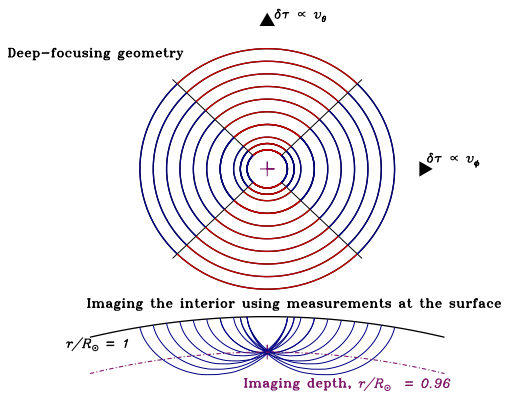

Fig. 2. The cross-correlation measurement geometry (upper panel; arrowheads - horizontal: longitude, and vertical: latitude) used to image the layer $r/R_\odot = 0.96$ (dot-dashed line). Doppler velocities of temporal length T measured at the solar surface are cross correlated between point pairs at opposite ends of annular discs (coloured red and blue); e.g., points on the innermost blue sector on the left are correlated with diagonally opposite points on the outermost blue sector on the right. Travel times of waves that propagate along paths in the direction of the horizontal and vertical arrows are primarily sensitive to longitudinal and latitudinal flows, v_ϕ and v_θ, respectively. The focus point of these waves is at $r/R_\odot = 0.96$ (lower panel) and the measured travel-time shift $\delta\tau(\theta, \phi, T)$ is linearly related to the flow component $v(r/R_\odot = 0.96, \theta, \phi)$ with a contribution from the incoherent wave noise. We are thus able to *map* the flow field at specific depths $v(r, \theta, \phi)$ through appropriate measurements of $\delta\tau(\theta, \phi, T)$.

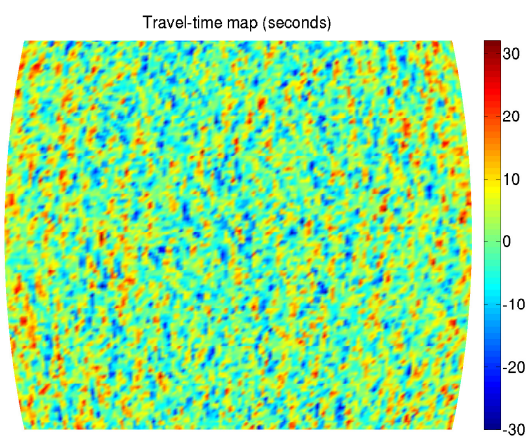

Fig. 3. A travel-time map spanning a $60^\circ \times 60^\circ$ region around the solar disk center, obtained by analyzing one day's worth of data taken by the Helioseismic and Magnetic Imager instrument [12] onboard the Solar Dynamics Observatory satellite. These times are so chosen as to be sensitive to flow systems in the solar interior. The spectrum of these travel times shows no interesting or anomalous peaks.

The variance of time shifts induced by convective structures that retain their coherence over timescale T does *not* diminish as T^{-1}, allowing us to distinguish them from noise. We may therefore describe the total travel-time variance $\sigma^2(T) \equiv \sum_{\theta,\phi} \langle \delta\tau^2(\theta, \phi, T) \rangle$ as the sum of variances of signal S^2 and noise N^2/T, assuming that S and N are statistically independent. Angled brackets denote ensemble averaging over measurements of $\delta\tau(\theta, \phi, T)$ from many independent segments of temporal length T. Given a coherence time $T_{\rm coh}$, we fit $\sigma^2(T) = S^2 + N^2/T$ over $T < T_{\rm coh}$ to obtain the integral upper limit S. The fraction of the observed travel-time variance that cannot be modeled as uncorrelated noise is therefore $S^2/\sigma^2(T_{\rm coh})$. For averaging lengths $T_{\rm coh}$ (= 24 and 96 hours) considered here, we find this signal to be small, i.e., $S^2 \ll N^2/T_{\rm coh}$, which leads us to conclude that large-scale convective flows are weak in magnitude. Further, since surface supergranulation contributes to S, our estimates form an upper bound on ordered convective motions.

Some details are in order. Spatial scales on spherical surfaces are well characterised in spherical harmonic space: $\delta\tau_{\ell m}(T) = \int_0^\pi \sin\theta \, d\theta \int_0^{2\pi} d\phi \; \delta\tau(\theta, \phi, T) \, Y^*_{\ell m}(\theta, \phi)$, where $Y_{\ell m}$ are spherical harmonics, (ℓ, m) are spherical harmonic degree and order, respectively, and $\delta\tau_{\ell m}(T)$ are spherical harmonic coefficients. Here, we specifically define the term "scale" to denote $2\pi R_\odot/\ell$, which implies that small scales correspond to large ℓ and vice versa. Note that a spatial ensemble of small convective structures such as a granules or inter-granular lanes (e.g., as observed on the solar photosphere) can lead to a broad power spectrum that has both small scales and large scales. The power spectrum of an ensemble of small structures, such as granulation patterns seen at the photosphere, leads to a broad distribution in ℓ, which we term here as *scales*. Travel-time shifts $\delta\mathcal{S}_{\ell m}$, induced by a convective flow component $v_{\ell m}(r)$, are given in the single-scattering limit by $\delta\mathcal{S}_{\ell m} = \int_\odot r^2 \, dr \, \mathcal{K}_\ell(r) \, v_{\ell m}(r)$, where $\mathcal{K}_\ell$ is the sensitivity of the measurement to that flow component. The variance of flow-induced time shifts at every scale is bounded by the variance of the signal in observed travel times, i.e., $\langle \delta\mathcal{S}^2_{\ell m} \rangle \leq S^2/\sigma^2(T_{\rm coh}) \, \langle \delta\tau^2_{\ell m}(T_{\rm coh}) \rangle$. To complete the analysis, we derive sensitivity kernels $\mathcal{K}_\ell(r)$ that allow us to deduce flow components in the interior, given the associated travel-time shifts (i.e., the *inverse* problem).

The time-distance deep-focusing measurement [13] is calibrated by linearly simulating waves propagating through spatially small flow perturbations, implanted at 500 randomly distributed (known) locations, on a spherical shell at a given interior depth (Figure 4). This delta-populated flow system contains a full spectrum and has power up to high spherical harmonic degrees. The simulated data are then filtered both spatially and temporally in order to isolate waves that

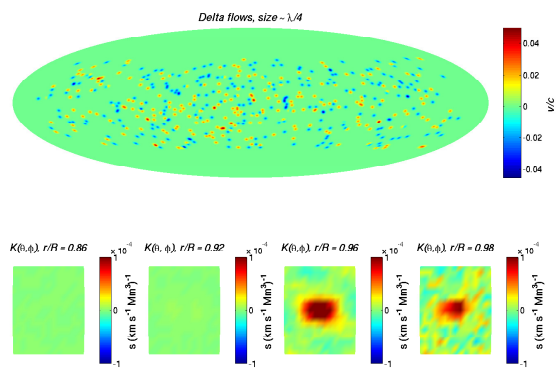

Fig. 4. Because wavelengths of helioseismic waves may be comparable to or larger than convective features through which they propagate, the ray approximation is inaccurate and finite-frequency effects must be accounted for when modeling wave propagation in the Sun [19]. In order to derive the 3D finite-frequency sensitivity function (kernel) associated with a travel-time measurement [20], we simulate waves propagating through a randomly scattered set of 500 east-west-flow 'delta' functions, each of which is assigned a random sign so as not to induce a net flow signal [18] (upper panel). We place these flow deltas in a latitudinal band of extent 120° centered about the equator, because the quality of observational data degrades outside of this region. We perform six simulations, with these deltas placed at a different depth in each instance, so as to sample the kernel at these radii. The bottom four panels show slices at various radii of the sensitivity function for the measurement which attempts to resolve flows at $r/R_\odot = 0.96$. Measurement sensitivity is seen to peak at the focus depth, a desirable quality, but contains near-surface lobes as well. Note that the volume integral of flows in the solar interior with this kernel function gives rise to the associated travel-time shift, which explains the units.

propagate to the specific depth of interest (termed phase-speed filtering). Travel times of these waves are then measured for focus depths the same as the depths of the features, and subsequently corrected for stochastic excitation noise [18]. Note that these corrections may only be applied to simulated data - this is because we have full knowledge of the realization of sources that we put in. Longitudinal and radial flow perturbations are analyzed through separate simulations, giving us access to the full vector sensitivity of this measurement to flows. Travel-time maps from the simulations appear as a low-resolution version of the input perturbation map because of diffraction associated with finite wavelengths of acoustic waves excited in the Sun and in the simulations. The connection between the two maps is primarily a function of spherical-harmonic degree ℓ. To quantify the connection, both images are transformed and a linear regression is performed between coefficients of the two transforms at each ℓ separately. The slope of this linear regression is the calibration factor for degree ℓ.

We apply similar analyses to 27 days of data (one solar rotation) taken by the Helioseismic and Magnetic Imager from June-July 2010. These images are tracked at the Carrington rotation rate, interpolated onto a fine latitude-longitude grid, smoothed with a Gaussian, and resampled at the same resolution as the simulations (0.46875 deg/pixel). The data are transformed to spherical harmonic space and temporal Fourier domain, phase-speed filtered (as described earlier) and transformed back to the real domain. Cross correlations and travel times are computed with the same programs as used on the simulations. Strips of 13 deg of longitude and the full latitude range are extracted from each of 27 days' results and combined into a synoptic map covering a solar rotation. The coefficients from the spherical harmonic transform of this map are converted, at each degree ℓ, by the calibration slope mentioned above, and a resultant flow spectrum is derived, as shown in Figure 5. These form observational upper bounds on the magnitude of turbulent flows in the convection zone.

It is seen that constraints in Figure 5 become poorer with greater imaging depth. This may be attributed to diffraction, which limits its seismic spatial resolution to a wavelength. In turn, the acoustic wavelength, proportional to sound speed, increases with depth. Since density also grows rapidly with depth, the velocity required to transport the heat flux of a solar luminosity decreases, a prediction echoed by all theories of solar convection. Thus we may reasonably conclude that the $r/R_\odot = 0.96$ curve is also the upper bound for convective velocities at deeper layers in the convective zone (although the constraint at $r/R_\odot = 0.92$ curve is weaker due to a coarser diffraction limit). Less restrictive constraints obtained at depths $r/R_\odot = 0.79, 0.86$ (whose quality is made worse by the poor signal-to-noise ratio) are not displayed here.

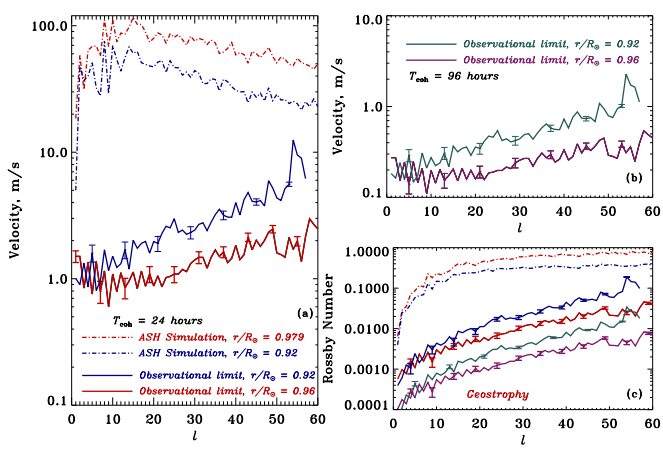

Fig. 5. Panels a, b: solid curves with 1-σ error bars show observational constraints on lateral flows averaged over m at radial depths, $r/R_\odot = 0.92, 0.96$; dot-dash lines are spectra from ASH convection simulations [6]. Colours differentiate between the focus depth of the measurement and coherence times. At a depth of $r/R_\odot = 0.96$, simulations of convection [6] show a coherence time of $T_{\rm coh} = 24$ hours (panel a) while MLT [14] gives $T_{\rm coh} = 96$ hours (panel b), the latter obtained by dividing the mixing length by the predicted velocity. Both MLT and simulations [21, 22] indicate a convective depth coherence over 1.8 pressure scale heights, an input to our inversion. At $r/R_\odot = 0.96$, MLT predicts a 60 $\mathrm{m\,s^{-1}}$, $\ell = 61$ convective flow and for $r/R_\odot = 0.92$, an $\ell = 33$, 45 $\mathrm{m\,s^{-1}}$ flow (upon applying continuity considerations [21]). Panel c shows upper bounds on Rossby number, $Ro = U/(2\Omega L)$, $L = 2\pi r/\sqrt{\ell(\ell+1)}$, $r = 0.92, 0.96 R_\odot$. Interior convection appears to be strongly geostrophically balanced on these scales. By construction, these measurements are sensitive to lateral flows i.e., longitudinal and latitudinal at these specific depths ($r/R_\odot = 0.92, 0.96$) and consequently, we denote these flows components (longitudinal or latitudinal) by scalars.

Implications

Convective transport. An ensemble of structures in the Sun of sizes small and large will result in a broad spectrum of flows as viewed in the space of spherical harmonics. Thus the large scales which we image here (i.e., power at low ℓ) contain contributions from small and large structures alike, and represent, albeit in a complicated manner, some features of the transport mechanism. Our constraints show that the kinetic energy associated with such an ensemble (at $r/R_\odot = 0.96$) is at most a thousandth of that of current models. Deeper within, i.e., $r/R_\odot < 0.96$, flows are likely to be even weaker due to the increasing density of the plasma. This represents a challenge to the mechanism of convective transport as discussed by e.g., [6]. We may further state, based on these observations, that *we do not definitively know* what the energy-carrying scales in the convection zone are. On a related front, how would this paradigm of turbulence in the convection zone affect extant theories of dynamo action?

For example, consider the scenario discussed by [23], who envisaged very weak upflows, which, seeded at the base of the convection zone, grow to ever larger scales due to the decreasing density as they buoyantly rise. These flows are in mass balance with cool intergranular plumes which, formed at the photosphere, are squeezed ever more so as they plunge into the interior. Such a mechanism presupposes that these descending plumes fall nearly ballistically through the convection zone, almost as if a cold sleet, amid warm upwardly diffusing plasma. In this schema, individual structures associated with the transport process would elude detection because the upflows would be too weak and the downflows of too small a structural size (M. Schüssler, private communication). When viewed in terms of spherical harmonics, the associated velocities at large scales (i.e., low ℓ), which contain contributions from both upflows and descending plumes, would also be small.

Differential Rotation. Differential Rotation, both a large-scale feature ($\ell \sim 2$) and large-sized structure since it is one individual global flow system, is easily detected in our travel-time maps. The stability and amplitude of this feature induces travel-time shifts whose variance does not change with the amount of temporal averaging T. The same is not true at related scales (i.e., $\ell < 60$), where the average variance of time shifts falls roughly like T^{-1}. Consequently, we may assert that we do not see evidence for a "classical" inverse cascade that results in the production of a smooth distribution of scales.

Further, the low Rossby numbers in our observations indicate that turbulence is geostrophically arranged on these scales at the depth $r/R_\odot = 0.96$. Because flow velocities are likely to become weaker deeper in the convection zone, the Rossby numbers will decrease correspondingly. At scales of $\ell < 60$, the Taylor-Proudman theorem describing geostrophic turbulence likely holds within most of the convection zone:

$$\Omega_0 \frac{\partial \Omega}{\partial z} = \frac{g}{2 C_p r^2 \sin\theta} \frac{\partial S}{\partial \theta}, \qquad [1]$$

where Ω_0 is the mean solar rotation rate, Ω is the differential rotation, z is the axis of rotation, θ is the latitude, g is gravity, S is the azimuthally and temporally averaged entropy gradient and C_p is the heat capacity at constant pressure. The rotation rate of the Sun is

helioseismically well constrained, i.e., the left side of equation (1) is accurately known. The iso-rotation contours are not co-aligned with the axis of rotation, implying a non-zero left side of equation (1). We may reasonably infer that the Sun does indeed possess a latitudinal entropy gradient, of a suitable form so as to sustain solar differential rotation. We do not speculate on the mechanism that may result in such a gradient.

ACKNOWLEDGMENTS. All computing was performed on NASA Ames supercomputers: Schirra and Pleiades. SMH acknowledges support from NASA grant NNX11AB63G and thanks Courant Institute, NYU for hosting him as a visitor. Warm thanks to M. Schüssler for useful conversations. T. Duvall thanks the Stanford solar group for their hospitality and J. Schou for helpful comments. Observational data that are used in our analyses here are taken by the Helioseismic and Magnetic Imager and are publicly available at http://hmi.stanford.edu/. We thank M. Miesch for sending us the simulation spectra. The authors declare that they have no competing financial interests. Correspondence and requests for materials should be addressed to S.M.H. (email: hanasoge@princeton.edu).

1. Stein RF, Nordlund Å (2000) Realistic Solar Convection Simulations. Solar Physics 192:91–108.
2. Vögler A, et al. (2005) Simulations of magneto-convection in the solar photosphere. Equations, methods, and results of the MURaM code. Astronomy and Astrophysics 429:335–351.
3. Rast MP (1998) Compressible plume dynamics and stability. Journal of Fluid Mechanics 369:125–149.
4. Miesch MS (2005) Large-Scale Dynamics of the Convection Zone and Tachocline. Living Reviews in Solar Physics 2:1.
5. Weiss A, Hillebrandt W, Thomas H, Ritter H (2004) Cox and Giuli's Principles of Stellar Structure (Cambridge Scientific Publishers), Second edition.
6. Miesch MS, Brun AS, De Rosa ML, Toomre J (2008) Structure and Evolution of Giant Cells in Global Models of Solar Convection. Astrophysical Journal 673:557–575.
7. Ghizaru M, Charbonneau P, Smolarkiewicz PK (2010) Magnetic Cycles in Global Large-eddy Simulations of Solar Convection. Astrophysical Journal Letters 715:L133–L137.
8. Hathaway DH, et al. (2000) The Photospheric Convection Spectrum. Solar Physics 193:299–312.
9. Duvall, Jr. TL, Jefferies SM, Harvey JW, Pomerantz MA (1993) Time-distance helioseismology. Nature 362:430–432.
10. Duvall, Jr. TL (2003) Nonaxisymmetric variations deep in the convection zone, ESA Special Publication ed Sawaya-Lacoste H Vol. 517, pp 259–262.
11. Gizon L, Birch AC, Spruit HC (2010) Local Helioseismology: Three-Dimensional Imaging of the Solar Interior. Annual Review of Astronomy and Astrophysics 48:289–338.
12. Schou J, et al. (2011) The Helioseismic and Magnetic Imager Instrument Design and Ground Calibration. Solar Physics p Submitted.
13. Hanasoge SM, Duvall TL, DeRosa ML (2010) Seismic Constraints on Interior Solar Convection. Astrophysical Journal Letters 712:L98–L102.
14. Spruit HC (1974) A model of the solar convection zone. Solar Physics 34:277–290.
15. Gough DO (1977) Mixing-length theory for pulsating stars. Astrophysical Journal 214:196–213.
16. Duvall, Jr. TL, et al. (1997) Time-Distance Helioseismology with the MDI Instrument: Initial Results. Solar Physics 170:63–73.
17. Gizon L, Birch AC (2004) Time-Distance Helioseismology: Noise Estimation. Astrophysical Journal 614:472–489.
18. Hanasoge SM, Duvall, Jr. TL, Couvidat S (2007) Validation of Helioseismology through Forward Modeling: Realization Noise Subtraction and Kernels. Astrophysical Journal 664:1234–1243.
19. Marquering H, Dahlen FA, Nolet G (1999) Three-dimensional sensitivity kernels for finite-frequency traveltimes: the banana-doughnut paradox. Geophysical Journal International 137:805–815.
20. Duvall, Jr. TL, Birch AC, Gizon L (2006) Direct Measurement of Travel-Time Kernels for Helioseismology. Astrophysical Journal 646:553–559.
21. Nordlund Å, Stein RF, Asplund M (2009) Solar Surface Convection. Living Reviews in Solar Physics 6:2.
22. Trampedach R, Stein RF (2011) The Mass Mixing Length in Convective Stellar Envelopes. Astrophysical Journal 731:78.
23. Spruit H (1997) Convection in stellar envelopes: a changing paradigm. Memorie della Societa Astronomica Italiana 68:397–408.